Research Article | Vol. 28, No. 12 / 8 June 2020 / Optics Express 17286
Optics EXPRESS

BER evaluation in a multi-channel graphene-silicon photonic crystal hybrid interconnect: a study of fast- and slow-light effects

JIE YOU,[1,4] ZILONG TAO,[2,4] YUKUN LUO,[1,4] JIE YANG,[1] JIANGHUA ZHANG,[1] XIN ZHENG,[1] XIANGAI CHENG,[3] AND TIAN JIANG[3,*]

[1]National Innovation Institute of Defense Technology, Academy of Military Sciences PLA China, Beijing 100071, China
[2]College of Computer, National University of Defense Technology, Changsha 410073, China
[3]College of Advanced Interdisciplinary Studies, National University of Defense Technology, Changsha 410073, China
[4]These authors contributed equally to this work
[*]tjiang@nudt.edu.cn

Abstract: A comprehensive theoretical investigation on the bit-error ratio (BER) performance of multi-channel photonic interconnects operating in pulsed regimes is presented. Specifically, the optical link contains either a silicon photonic crystal (SiPhC) or a SiPhC-graphene (SiPhC-GRA) waveguide, possessing slow-light (SL) and fast-light (FL) regimes. A series of Gaussian pulses plus complex white noise are placed at input of each channel, with output signals demultiplexed and analyzed by a direct-detection receiver. Moreover, a rigorous theoretical model is proposed to measure signal propagation in SiPhC and SiPhC-GRA, which incorporates all crucial linear and nonlinear optical effects, as well as influences of free-carriers and SL effects. BER results of multi-channel systems are evaluated by utilizing the Fourier series Karhunen-Loeve expansion method. Our findings reveal that good BER performance is acquired at SiPhCs and SiPhC-GRAs in SL regimes but with their footprint about 2.5-fold smaller than FL waveguides. Moreover, the enhanced nonlinearity in SiPhC-GRAs induced by strong graphene-SiPhC coupling causes extra signal degradation than SiPhCs at the same length. This work provides additional insights into the coupling effect between SiPhCs operating in SL regimes and graphene, and their influence on WDM signal transmission, highlighting the potential applications of SiPhC-GRA interconnects in next-generation super-computing systems.

1. Introduction

Photonic networks with small footprint and low power consumption have established as a promising and appealing solution for the rapidly increasing bandwidth demands created by supercomputers, cloud data centers and internet-related industries [1–3]. After showing great potentials in replacing copper wires [4], optical interconnects with ultrawide bandwidth and extremely fast processing speed are envisioned to play more significant role in communications at extremely small scale, including the infrastructures of board-to-board, node-to-node and even chip-to-chip [5]. Silicon-on-insulator (SOI) material platform is viewed as one of the most successful techniques to seamlessly implement optics into the chip-level communication networks [6]. Especially, silicon (Si) photonic crystal (SiPhC) waveguide [7], which contains a line defect in its periodic dielectric matrix, has exhibited distinguished optical properties encompassing high index contrast [8], broadband transparency window [9], large dispersion and nonlinearity [10], and good compatibility with CMOS electric circuitries [11].

#392907 https://doi.org/10.1364/OE.392907
Journal © 2020 Received 17 Mar 2020; revised 3 May 2020; accepted 13 May 2020; published 26 May 2020

Optics EXPRESS

Apart from the direct application of optical waveguides [12,13], SiPhCs also enable various nonlinear functionalities, such as optical modulators [14], amplifiers [15], receivers [16], frequency converters [17], and optical switches [18,19]. Moreover, SiPhCs allow for the engineering of group-velocity (GV) of the propagating optical signals from the fast-light (FL) to slow-light (SL) [20] regimes, causing a significant change in the waveguide dispersion and nonlinearity. More specifically, optical losses [21], GV dispersion (GVD) [22], self-phase modulation (SPM) [23], cross-phase modulation (XPM) [24], and two-photon absorption (TPA) [25], are enhanced in SL regimes, leading to the degradation of signal quality, which in turn reduces the characteristic lengths of dispersion and nonlinearity, as well as the device footprint. In multi-channel SiPhCs, free-carriers (FCs) induce additional signal cross-talk, whose detrimental strength is further enhanced in SL regions [26]. However, the advancement of SL effects in multi-channel photonic systems is still not clear and worthy of scholar attention.

The one-atom-thick graphene, serving as an important family of two-dimensional (2D) materials, has gained vast popularity in many fields, including electronics [27], membranes [28], biomedical devices [29], sensors [30], energy harvesting and storage [31], beam manipulation [32,33], phase resonance tuning [34], and composites and coatings [35], which is attributed to its distinguished mechanical, thermal, electronic, and optical properties [36,37]. Specifically, zero bandgap [38], large thermal conductivity [39], high carrier mobility [40], and tunable chemical potentials [41] grant graphene great potentials for applications in active, ultrafast photonic devices and electronic circuits at an extremely small scale. From a new aspect, graphene has been theoretically and experimentally proved to own an exceedingly large nonlinear refractive index [42,43], facilitating enormous possibilities for the innovations of graphene-based nonlinear nanodevices. Thus, the integration of graphene with semiconductors or other 2D materials has established as an exciting and intriguing route for chip-level device fundamentals and applications. Despite graphene-Si hybrid waveguides being intensively explored in the last decade [44,45], it is still not transparent how the interaction between graphene and SiPhC in SL regime would affect practical applications of Si-graphene hybrid devices, especially in the case of WDM data transmission whose signal is modulated by the return-to-zero (RZ) format. RZ refers to a format of signal transmission where the low and high states are represented by "0" and "1", whose resting state during the second half of each bit is usually zero. Notably, RZ signals are more often used in communication systems than the nonreturn-to-zero format, since the former is more tolerant to optical nonlinearity and dispersion [46].

Herein, a theoretical investigation is conducted to study the transmission bit-error ratio (BER) of multi-channel RZ photonic systems. Importantly, BER represents the number of bit errors divided by the total transmitted bit number in a time interval. The investigated system consists of an array of lasers serving as optical sources for $\tilde{N}$ communication channels, a multiplexer, a Si-based photonic interconnect consisting of either a SiPhC waveguide or a SiPhC-graphene (SiPhC-GRA) hybrid waveguide, a demultiplexer, and a direct-detection receiver for the central channel (see Fig. 1). The input is a superimposition of $\tilde{N}$-channel ON-OFF keying (OOK) RZ modulated Gaussian pulses in a 512-bit pseudorandom binary sequence (PRBS) pattern, with the ON and OFF power states of P and zero, accompanied by complex white noise. In order to describe the signal evolution, a rigorous theoretical model based on the nonlinear Schrodinger equations (NLSEs) is introduced, which measures all key linear and nonlinear optical effects, as well as the FCs' influences. Furthermore, the transmitted BERs in the central channel is evaluated by utilizing the Fourier series Karhunen-Loeve series expansion (KLSE) method in coupled with a perturbation theory. This work addresses a neglected aspect of SL effect in SiPhC-GRA and its advantages for the multi-channel signal processing, promoting SiPhC-GRAs' practicability in chip-level device fundamentals and applications.

Optics EXPRESS

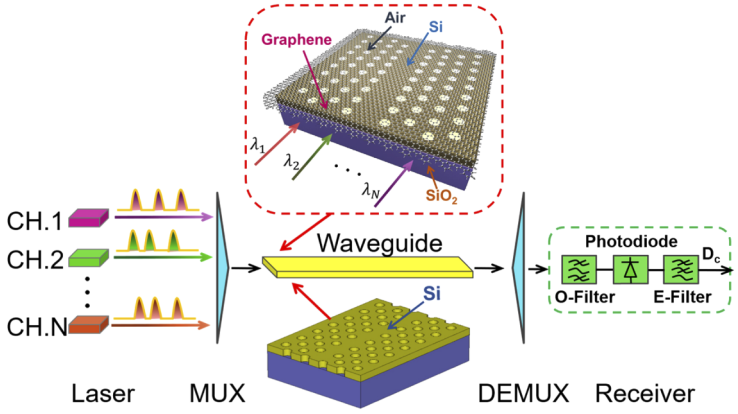

Fig. 1. Schematic illustration of a multi-channel photonic system, which contains multiple lasers with different wavelengths, a multiplexer, a photonic interconnect, a demultiplexer and a direct-detection receiver for the central channel. Specifically, both a SiPhC waveguide possessing the FL and SL regimes, and a SiPhC-GRA hybrid waveguide are utilized in this system. The receiver consists of a bandpass optical filter H_o, a photodiode, and an electrical lowpass filter H_e.

2. Theoretical models

2.1. Signal propagation in Si-based photonic waveguides

A rigorous theoretical model consisting of an array of coupled NLSEs and a rate equation governing the FC dynamics is introduced to characterize the multi-wavelength optical pulse propagation in SiPhC and SiPhC-GRA, as well as the mutual interaction between optical pulses and FCs, which is explicitly expressed as [26],

$$\frac{\partial \mathrm{A}_m}{\partial z} + \left(\frac{1}{v_{g,m}} - \frac{1}{v_{g,c}}\right)\frac{\partial \mathrm{A}_m}{\partial T} + i\frac{\beta_{2,m}}{2}\frac{\partial^2 \mathrm{A}_m}{\partial T^2} = \frac{i\omega_m \kappa_m}{n v_{g,m}}\delta n_{fc}\mathrm{A}_m - \frac{c\kappa_m}{2n v_{g,m}}(\alpha_{in} + \alpha_{fc})\mathrm{A}_m + i\left(\gamma_m|\mathrm{A}_m|^2 + 2\sum_{j\neq m}\gamma_{mj}|\mathrm{A}_j|^2\right) \tag{1a}$$

$$\frac{\partial N}{\partial z} = -\frac{N}{\tau_0} + \sum_{m,j} D_{mj}|\mathrm{A}_m|^2|\mathrm{A}_j|^2 \tag{1b}$$

Unless other places are specified, all the simulations are taken from the 1st to $\tilde{N}$th channel. Here, $\mathrm{A_m}$ (z, T) is the pulse envelop for the mth wavelength, in unit of $\sqrt{\mathrm{W}}$, where z and T are the propagation length and the time in the central channel moving with velocity $v_{g,c}$, respectively. Notably, $T = t\text{-}z/v_{g,c}$, with t to be the physical time. Take the mth channel for instance, $\beta_{2,m}$ is the GVD coefficient, ω_m is the carrier frequency, κ_m is the overlap between the optical mode and waveguide active area and α_{in}=50 dB/cm is the intrinsic loss [47–49]. Additionally, γ_m and γ_{mj} are the third order nonlinear coefficients, with γ_{mj} capturing the coupling effect between mode m and mode j. In terms of FCs, δn_{fc} and α_{fc} are the FC-induced refractive index change and FC absorption (FCA) coefficient, respectively, τ_0 is the FC relaxation time, which is assumed to be 0.5 ns [50]. Furthermore, the key parameters D_{mj} describe the transfer rate of the energy from the optical field to FCs, which are given by,

$$D_{mj} = \begin{cases} \frac{\gamma''_m}{\hbar\omega_m A_{eff}}, m = j \\ \frac{4\gamma''_{mj}}{\hbar(\omega_m+\omega_j)A_{eff}}, m \neq j \end{cases} \tag{2}$$

Optics EXPRESS

Here, A_{eff} is the effective mode area where FCs are generated, which is set to $A_{eff}=a\times h$ for SiPhCs and SiPhC-GRAs. More rigorous definitions regarding A_{eff} can be found in [51]. It is important to stress that the model in Eq. (1) is appliable to both SiPhC and SiPhC-GRA, since the core of SiPhC-GRA is basically Si, in which the signal propagation is in presence of FCs. In this context, the symbol $\zeta'(\zeta'')$ stands for the real (imaginary) part of the complex number ζ.

2.2. Characterization of photonic waveguides

In this work, two types of photonic waveguides are investigated, with their schematics being illustrated in the central section of Fig. 1. More specifically, the first waveguide is a SiPhC containing a line defect in a 2D hexagonal lattice of air holes in a Si slab, as shown in Fig. 1. Its typical dimensional parameters include the lattice constant a, the thickness h, and the hole radius of r=0.22a. The other one is a SiPhC-GRA waveguide, which contains a monolayer graphene covering the surface of SiPhC. This enables the exploration of strong interaction between SiPhC and graphene, and the nonlinearity enhancement. Though the core material of Si photonic waveguides makes the dominant contribution to the nonlinear effects, it is no longer suitable to characterize the optical nonlinearity inside SiPhC-GRAs. This is because graphene possesses the one-atom-thickness and large nonlinear refractive index. In this context, the SiPhC-GRA waveguides are proposed to maximize the waveguide nonlinear parameters, allowing for new applications that require strong third-harmonics generation, four-wave mixing, Kerr effects, and pulse compression at a significantly reduced power level.

The photonic band structure of SiPhC is shown in Fig. 2(a), where two guiding modes are observed. Notably, all shaded areas in Fig. 2 represent the SL spectral regions. Particularly, the mode A owns two SL spectral regimes while mode B only possesses one. The third order nonlinearity of SiPhCs is determined by γ, which is mathematically expressed as,

$$\gamma = \frac{3\omega\varepsilon_0 a}{16 v_g^2}\frac{\Gamma}{W^2} \tag{3}$$

where Γ is the mode mediated scalar third order nonlinear susceptibility, and W is the optical energy of the optical mode contained in the unit cell of SiPhC waveguides [26].

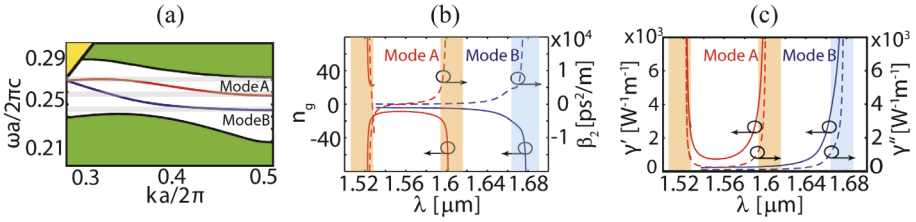

Fig. 2. (a) Mode dispersion diagram of the SiPhC waveguide. Notably, the yellow and green areas represent the leaky and guiding modes, respectively. (b)-(c) Wavelength dependence of n_g, β_2, γ' and γ''calculated for mode A (red curves) and mode B (blue curves). Here, all shaded areas indicate the SL spectral domains defined as n_g>20.

Obviously, it is seen from Figs. 2(b) and 2(c) that in the SL region, the group index, $n_g=c/v_g$, the GVD coefficient β_2, the nonlinear coefficients γ' and γ'' are much larger compared to the FL region, indicating that the linear and nonlinear optical responses are strongly enhanced in SL regime. This is because the GVD and waveguide nonlinearity are proportional to the quantities of v_g^{-1} and v_g^{-2}, respectively. Furthermore, as indicated in Fig. 2(a), it is possible to tailor the dispersion of mode A from normal to anomalous regions by changing the lattice constant but keeping $\omega a/2\pi c = a/\lambda$ constant. Based on this, we designed the SiPhC waveguides that possess either normal or anomalous dispersion at the telecommunication wavelength 1550 nm (i.e., central

Optics EXPRESS

channel), as well as the FL and SL spectral regions, which allows for the exploration of dispersion influence on the system performance. Thus, in all investigated multi-channel systems, SiPhC waveguides are divided into two categories, namely the type 1 waveguide (λ_c=1550 nm, β_2<0) and type 2 waveguide (λ_c=1550 nm, β_2>0). All relative parameters for SiPhC waveguides in the central channel are described in Table 1, which are derived by using the MPB algorithm [52].

Table 1. Linear and nonlinear optical parameters for investigated photonic waveguides

Waveguide Type	λ_c [nm]	a [nm]	n_g	β_2 [ps^{2}m^{-1}]	κ	γ' [W^{-1}m^{-1}]	γ'' [W^{-1}m^{-1}]
SiPhC-FL-1	1550	412	8.91	-330.75	0.9937	724.26	220.7
SiPhC-FL-2	1550	406	9.28	368.30	0.9919	1102.9	336.1
SiPhC-GRA-FL-1	1550	412	8.91	-330.75	0.9937	1336.2	336.8
SiPhC-GRA-FL-2	1550	406	9.28	368.30	0.9919	2080.5	513
SiPhC-SL-1	1550	419	22.40	-1.76 ×10^4	0.9954	4388.1	1337
SiPhC-SL-2	1550	400	20.19	6.36 ×10^4	0.9902	6608.6	2014
SiPhC-GRA-SL-1	1550	419	22.40	-1.76 ×10^4	0.9954	8208.3	2019.7
SiPhC-GRA-SL-2	1550	400	20.19	6.36 ×10^4	0.9902	1.24 ×10^4	3041.7

In order to characterize optical properties of SiPhC-GRA waveguides, we should first proceed with the surface quantities of graphene. Particularly, the sheet conductivity σ_s can be used to depict the light-graphene interaction, which is expressed as [53],

$$\frac{\sigma_s(\omega)}{\sigma_0} = \frac{4\varepsilon_F}{\pi\hbar}\frac{\tau}{1-i\omega\tau} + \theta(\hbar\omega - 2\varepsilon_F) + \frac{i}{\pi}\ln\left|\frac{\hbar\omega - 2\varepsilon_F}{\hbar\omega + 2\varepsilon_F}\right| \tag{4}$$

Here, $\sigma_0=e^2/(4\hbar)$ represents the universal dynamic conductivity of graphene, e is the single charge, $\hbar$ denotes the reduced Planck constant, θ is a Heaviside step function, $\varepsilon_F = 0.6$ eV is the Fermi level, and $\tau = 0.25$ ps/2π is the relaxation time [39,54,55]. Notably, such settings ensure the graphene sheet in the plasmonic regime, allowing for the coupling effect between surface plasmonic polaritons of graphene and the SiPhC. Thus, the graphene's wavelength dependence of σ_s is shown in Fig. 3(a). Precisely, σ_s is composed of the intraband (Drude) part corresponding to the first term on the right of Eq. (4), and the interband part relative to the following two terms. Considering that the nonlinear effects in SiPhC-GRAs are affected by the optical nonlinearity of graphene, the nonlinear optical conductivity of graphene is worthy of studying. Assuming that electron-electron and electron-photon scattering as well as thermal effects are neglectable, the nonlinear optical conductivity of graphene σ_3 is defined as [39,56],

$$\sigma_3(\omega) = \frac{i\sigma_0(\hbar v_F e)^2}{48\pi(\hbar\omega)^4}\mathbb{R}\left(\frac{\hbar\omega}{2\varepsilon_F}\right) \tag{5}$$

Here, $\mathbb{R}(x) = 17G(x)-64G(2x)+45G(3x)$, $G(x)=\ln|(1+x)/(1-x)|+i\pi\theta(|x|-1)$, $v_F=3a_0r_0/(2\hbar)$ is the Fermi velocity, a_0=1.42 Å is the distance between the two adjacent carbon atoms in graphene, and r_0=2.7 eV is the nearest-neighbor coupling constant. The curves of σ_3 is presented in Fig. 3(b), which is directly related to the effective third-order nonlinear susceptibility of graphene.

To this point, the third order nonlinearity of SiPhC-GRA waveguides can be calculated using the following relation [44],

$$\gamma = \frac{2\pi}{\lambda}\frac{\iint_D s_z^2\chi^{(3)}(x,y)dxdy}{\left(\iint_D s_z dxdy\right)^2} \tag{6}$$

Here, s_z denotes the time-averaged Poynting vector, D represents the core and cladding areas that contain a propagating electrical field intensity, and $\chi^{(3)}$ is the third-order nonlinear susceptibility.

Optics EXPRESS

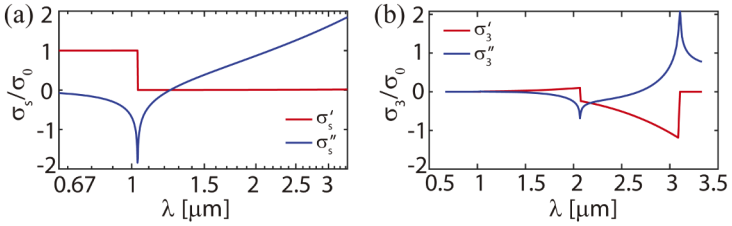

Fig. 3. (a) Spectral dependence of the complex sheet conductance of graphene, σ_S, with the wavelength ranging from visible to mid-Infrared regions. (b) The third-order nonlinear surface conductivity of graphene, σ_3. The red curves represent the real part, while the blue ones are the imaginary part for all cases.

Thus, the nonlinear parameters of SiPhC-GRA can be computed according to Eq. (6), with waveguide coefficients of SiPhC-GRA at 1550 nm being presented in Table 1.

A vivid illustration of the time evolution for 10-channel noise-free optical signals propagating in the type 2 waveguides of SiPhC and SiPhC-GRA that possess normal dispersion, is presented in Fig. 4, with the bit sequence being "10001011" for each channel. One remarkable but not surprising finding is that the optical signals exhibit a more significant degradation in SL waveguides than the FL ones at the same length, in cases of SiPhCs and SiPhC-GRAs. This is because the SL waveguide possesses larger nonlinearity than the FL waveguide, which would induce the enhanced FCA, TPA and cross-absorption modulation that are responsible for the severe signal degradation. Though not that obvious, the SiPhC-GRAs induce additional signal distortion when compared to SiPhCs, which is caused by the strong coupling effect between monolayer graphene and SiPhCs and the resulting enlarged nonlinear parameters. Alternatively, the signal quality at the output of type 2 SL waveguides (L=200 μm, P=0.41P_0 or P=0.38P_0) are comparable to that in type 2 FL waveguides (L=500 μm, P=0.42P_0 or P=0.40P_0), in cases of with and without graphene monolayer integrated. The dynamics of FC carriers for SiPhC-FL-2, SiPhC-GRA-FL-2, SiPhC-SL-2, and SiPhC-GRA-SL-2 are shown in Figs. 4(e), 4(f), 4(g), and 4(h), respectively. It is seen form these figures that approximately 2-fold of FCs densities are generated in SiPhC-GRAs when compared with SiPhCs, valid for both FL and SL regimes. Moreover, due to the enhanced nonlinear optical effects in the SL regions, their densities of FCs are about 7-fold larger than FL regions, accounting for both SiPhC and SiPhC-GRAs.

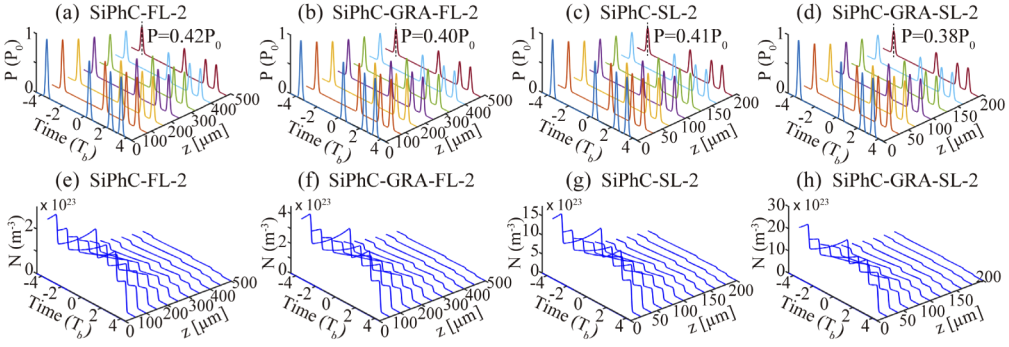

Fig. 4. (a)-(d) Time domain and (e)-(h) carrier density evolution of a 8-bit noisy-free Gaussian pulsed signal with average power P=10 mW and bit window T_b=100 ps in 10-channel photonic waveguides operating in FL and SL regimes. From left to right, the panels correspond to waveguides of SiPhC-FL-2, SiPhC-GRA-FL-2, SiPhC-SL-2, and SiPhC-GRA-SL-2.

Optics EXPRESS

2.3. BER calculation for multi-channel RZ pulsed signals

A Fourier series KLSE approach [57] is proposed to calculate system BER for multi-channel photonic systems, similar to the single channel detection case [58]. Additionally, a perturbation theory is utilized to quantify the transmission matrix and the noise correlation matrix [59] in the central channel. Here, input signals are a train of OOK modulated Gaussian pulses in a 512-bit PRBS pattern, in presence of complex additive white noise. Notably, the central channel is referred as the qth channel for $\tilde{N}$-channel systems, with q equaling to $(\tilde{N}+1)/2$ $(\tilde{N}/2)$ when $\tilde{N}$ is odd (even). This algorithm is also applicable to single-channel case, under condition of $q=\tilde{N}=1$.

To start with, the optical pulsed field of qth channel at the front-end of the waveguide is expressed as $u_q(t)=s_q(t)+a_q(t)$, with $s_q(t)$ and $a_q(t)$ to be noise-free Gaussian pulses and complex additive white noise. Particularly, by using the Fourier series expansion, the noise term is written in $a_q=\sum n_{q,p}\cdot\exp(i\Omega_p t)$, where $\Omega_p=2\pi p/T_c$ and $T_c=N_b\cdot T_b$, with $p\in[-N_b/2, N_b/2-1]$, N_b to be total number of transmitted bits, and T_b being the bit window. Next, the real noise Fourier vector is acquired, which is denoted as $\underline{\tilde{a}}_q=(n'_{q,-M},\ldots,n'_{q,M}, n''_{q,-M},\ldots, n''_{q,M})^{\mathrm{T}}$, where the symbol $^{\mathrm{T}}$ represents transposition. The relatively small value of M compared to N_b is selected to relieve the computational burdens. Regarding the noise covariance matrix $\underline{\underline{R}}^q=<\underline{\tilde{a}}_q\underline{\tilde{a}}_q{}^{\mathrm{T}}>$, it can be computed by combining the transmission matrix $\underline{\underline{\mathrm{H}}}$ with the initial covariance matrix $\underline{\underline{R}}^q(0)$, namely, $\underline{\underline{R}}^q(L)=\underline{\underline{\mathrm{H}}}\ \underline{\underline{R}}^q(0)\ \underline{\underline{\mathrm{H}}}^T$. Then, our emphasis shifts to the derivation of $\underline{\underline{\mathrm{H}}}$ via a perturbation theory. We assume that the coupling effects between the noise in the central channel and that in the rest channels can be neglected, so we only compute the covariance matrix for the central channel. Specifically, in the central channel of waveguides, the noise free Gaussian pulses $s_q{}^0(t,0)$ is perturbed by a small quantity $\eta\cdot\exp(i\Omega_{\varpi-M-1}t)$ at the ϖ-th frequency, where $\eta\ll 1$ and $\varpi\in[1, 2M+1]$. Thus, the perturbed pulsed signal is given by,

$$s_q^{\varpi}(t,0)=s_q^0(t,0)+\eta\exp(i\Omega_{\varpi-M-1}t) \tag{7}$$

After propagating through the photonic waveguides using Eq. (1), the output Gaussian pulse in the central channel, $s_q{}^{\varpi}(t, L)$, is obtained. What follows is to compute the Fourier coefficients vector $\underline{\upsilon}^{\varpi}$ for the quantity $\Delta s_q{}^{\varpi}(t)=s_q{}^{\varpi}(t, L)-s_q{}^0(t, L)$. This allows for the extraction of the transmission matrix $\underline{\underline{\mathrm{H}}}$, whose element is expressed as follows:

$$\underline{\underline{\mathrm{H}}}^{\xi\varpi}=\underline{\upsilon}_{\xi}^{\varpi}\Big/\eta \tag{8}$$

where $\xi\in[1, 4M+2]$. Please note that η is a real positive number if $\xi\le(2\mathrm{M}+1)$, otherwise η is a positive imaginary number. Thus, the $(4M+2)\times(4M+2)$ real transmission matrix $\underline{\underline{\hat{\mathrm{H}}}}$ is acquired by expanding the $(4M+2)\times(2M+1)$ complex matrix $[\underline{\underline{\mathrm{H}}}$ to $\underline{\underline{\hat{\mathrm{H}}}}]=\underline{\underline{\mathrm{H}}}', \underline{\underline{\mathrm{H}}}''$. Finally, the noise covariance matrix $\underline{\underline{R}}^q(L)$ is addressed, since its initial matrix $\underline{\underline{R}}^q(0)$ can be directly computed from the input white noise. Particularly, the interaction between the noises in the central channel with the noise-free signal in all channels is considered, since the noise evolution at each frequency is calculated in presence of $\tilde{N}$ channels.

Another important aspect is utilizing the Fourier series KLSE approach to compute system BER at the output of the receiver. One key point of this detection strategy is that the surrounding $\tilde{N}$-1 ($\tilde{N}>1$) channels are filtered out before entering the receiver, since they would otherwise cause the phase distortion in the central channel [60], coincided with the receiver setup in Fig. 1. The first step is to describe photocurrent $y_q(t)$ in a double Fourier transform,

$$y_q(t)=\int\!\!\int_{\infty}U_q^*(\omega_m)\underline{\underline{\Theta}}(\omega_m,\omega_k)U_q(\omega_k)e^{i(\omega_k-\omega_m)t}d\omega_m d\omega_k \tag{9}$$

Here, $U_q(\omega)$ is the Fourier transform of the input pulsed signals for the receiver, and $\underline{\underline{\Theta}}(\omega_m,\omega_k)=H_o{}^*(\omega_m)\,H_e(\omega_m-\omega_k)\,H_o(\omega_k)$ is the Hermitian kernel, with $H_o(\omega)$ and $H_e(\omega)$ to be the Fourier

Optics EXPRESS

transform of optical and electric filters. Next, the receiver matrix is written in a new form of $\underline{\underline{\Xi}}$ =[$\underline{\Theta'}$, $\underline{\Theta''}$; $\underline{\Theta''}$, $\underline{\Theta'}$], ensuring that all elements are real. Moreover, the moment-generating function (MGF) of $\overline{y_q(t)}$ is calculated, in which the Cholesky factorization is utilized to decompose the noise covariance matrix and then an orthogonal matrix is employed to diagonalize the correlation matrix consisting of receiver matrix and noise covariance matrix [58]. Importantly, the dimension of the correlation matrix is (4M+2) ×(4M+2). Thus, the MGF of $y_q(t)$ is mathematically expressed as,

$$\Psi_{y_q}(s) = \prod_{k=1}^{4M+2} \frac{\exp\left(\frac{\rho_k |\vartheta_m|^2 s}{\sqrt{1-2\rho_k s}}\right)}{\sqrt{1-2\rho_k s}} \tag{10}$$

where ρ_k are the eigenvalues of the correlation matrix, and ϑ_m are the transformed signals for $y_q(t)$, detected at the middle of each bit interval t_m. Finally, the system BER is computed via the following relation,

$$\mathrm{P} = \frac{1}{2}\left[\mathrm{P}(y_q > y_{th,q} | u_q = 0) + \mathrm{P}(y_q < y_{th,q} | u_q = \sqrt{P_q})\right] \tag{11}$$

where the first (second) term stands for the error occurrence probability when "0" ("1") bits are transmitted in the qth channel, and $y_{th,q}$ is the corresponding threshold for detection. These probability density functions are obtained by performing Riemann-Fourier inversion [61] on the MGFs, which can be further simplified by utilizing the saddle-point approximation [57]. More details for signal detection algorithm are reported in [58].

3. Results and discussion

For a better illustration for the application of our theoretical models in the practical communication systems, we consider a $\tilde{N}$-channel ($\tilde{N}$ = 1-8) OOK system (λ_c=1550 nm) operating in the RZ regime, with the signal bit rate remaining unchanged at B_r = 10 Gb/s (bit window T_b=100 ps) and the signal pulsewidth of T_p=20 ps. A PRBS of Gaussian pulses with 2^9-1 bits and a zero bit are utilized in this work, encompassing all possible patterns for 9-bit sequence. Additionally, we select the average power of P=10 mW for the input pulses, which is in a similar power level as the recent experimental study of the multi-channel Si-based waveguides [22]. Two types of photonic waveguides, SiPhC and SiPhC-GRA, which possess both FL and SL regions, as well as normal and anomalous dispersions, are investigated in this work (see Table 1), with the length of FL and SL waveguides to be L=500 μm and L=200 μm, unless otherwise specified. Regarding the direct-detection receiver, the 3-dB bandwidth of an electrical filter is B_e=10 Gb/s, while the optical filter is equipped with a 3-dB bandwidth B_o that satisfies B_o=4B_e.

One important factor that most influences the transmission BER is the GV, since it determines the strength of linear and nonlinear optical effects that affect the propagating signals. As shown in Fig. 2(a), it is feasible to alter v_g from the FL to SL regime by simply changing the signal frequency. Thus, we begin to investigate the system performance in the multi-channel SiPhC-FLs and SiPhC-GRA-FLs interconnects with both normal and anomalous dispersion, accounting for the various number of channels and input signal-to-noise ratio (SNR). Note that SNR is defined as the ratio between the power of Gaussian pulses and the average of the powers of the complex white noise in this work. In Fig. 5, we plot the BERs in the central channel of various FL systems whose number of channels changes from 1 to 8. One significant finding of the WDM photonic systems is that the BER increases significantly with the number of channels, which is more obvious in cases of SiPhC-GRA-FLs. This phenomenon is expected, since the influence of inter-channel interactions induced by nonlinear effects and FCs is enhanced when the number of channels turns larger. In terms of the SiPhC-FL waveguides, the BER performance in anomalous dispersion (type 1, left) region is much better than that in normal dispersion (type 2,

Optics EXPRESS

right) regime, which can be explained by the fact that the nonlinearity of SiPhC-FL-2 is almost 2-fold larger than SiPhC-FL-1. This conclusion is also applicable to the SiPhC-GRA-FLs with these two dispersion regimes. Furthermore, in comparison with the SiPhC-FL waveguides, the SiPhC-GRA-FL waveguides have a far worse system BERs, which is attributed to the coupling effect between the surface plasmonic polaritons of graphene and the optical modes of SiPhC-FLs and the resulting enhanced optical nonlinearity.

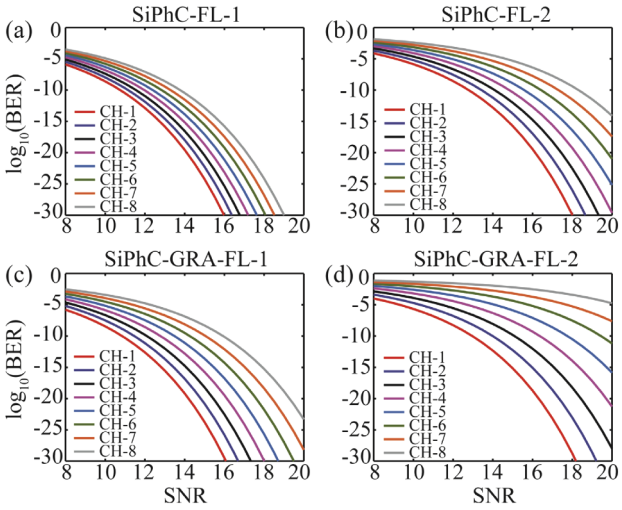

Fig. 5. System BER versus SNR, calculated for two types of multi-channel Si-based photonic systems operating in FL spectral regions. Here, the number of channels varies from 1 to 8. The investigated waveguides and their lengths are SiPhC-FL (top, 500 μm) and SiPhC-GRA-FL (bottom, 500 μm). The left panels correspond to the type 1 waveguides, whereas the right ones represent type 2 waveguides. In all simulations, P=10 mW, B_r=10 Gb/s, T_p = 20 ps.

Alternative insights into the contribution of nonlinear effects to the system performance are furnished by the BER evaluation in the multi-channel SL waveguides. As presented in Fig. 6, apparently, the BERs in both SiPhCs and SiPhC-GRAs operating in SL regimes are comparable to the cases of FL regions shown in Fig. 5 to some extent, which indicates that an excellent system performance can be obtained in the multi-channel SL interconnects provided that their length is properly reduced. Moreover, the difference between BER curves in the normal (type 2) and anomalous (type 1) regions is much larger than that in SiPhC-FLs and SiPhC-GRA-FLs, which is caused by the enhancement of the dispersion and optical nonlinearity, leading to a larger BER variation with number of channels. On the other hand, it is found that transmission BERs in the normal dispersion regions (type 2) of SiPhC-SLs and SiPhC-GRA-SLs are significantly smaller than the anomalous regions (type 1), while the opposite situation is observed in the FL cases, accounting for different number of channels. Particularly, due to the enlarged optical nonlinearity in the SiPhC-GRA-SLs, the overall BER is not as good as SiPhC-SLs. Also, it should stress that transmission BER exhibits the strongest variation with number of channels in cases of SiPhC-GRA-SLs.

In other aspect, it is noticeable that the type 1 and type 2 of SiPhC-FL and SiPhC-SL waveguides in Table 1 are associated with different dispersion regimes and different GV. As mentioned earlier, it is achievable to tune the waveguide from the FL to SL regimes by moving the point (fixed at a/λ) from the un-shaded regions to the shaded areas of Mode A. Hence, if the wavelength remains at 1550 nm, the lattice constant would vary accordingly. Moreover, it is easily validated that in SiPhCs β_2 and γ are proportional to a and a^{-3}, respectively. This means that for a specific

Optics EXPRESS

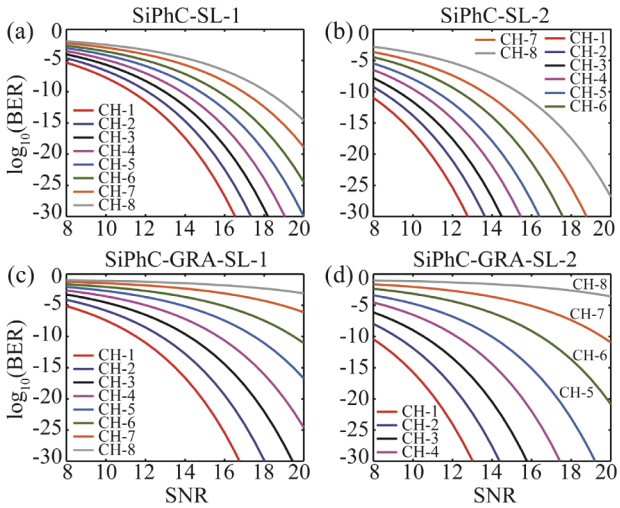

Fig. 6. System BER versus SNR, calculated for two types of Si-based photonic systems operating in SL regimes, accounting for the number of channels changing from 1 to 8. From top to bottom, the panels correspond to SiPhC-SL (200 μm) and SiPhC-GRA-SL (200 μm), respectively. Here, the solid lines in left panels stand for the type 1 waveguides, while the curves in right panels represent type 2 waveguides. In all cases, P=10 mW, B_r=10 Gb/s, $T_p = 20$ ps.

wavelength, β_2 increases with a larger a, while the opposite case is true for γ. The degradation rate of γ with a is much faster than the increase rate of β_2, and vice versa. When considering the waveguides of SiPhC-GRAs, their GVD and partial nonlinearity from SiPhC contributions also satisfy the above relation pertaining to lattice constant. Thus, the waveguide nonlinearity of SiPhC-GRA waveguides will increase significantly with a smaller lattice constant, especially under the coupling effect between graphene and SiPhCs. These facts are responsible for the variation of BER in different multi-channel systems presented in Fig. 5 and Fig. 6.

4. Summary

In conclusion, we have established a complicated theoretical and numerical study of the BER performance for multi-channel photonic systems working in the pulse regime. We have included two types of Si-based photonic waveguides, which are a SiPhC waveguide a a monolayer graphene-SiPhC integrated waveguide, providing efficient communication platforms for multi-wavelength Gaussian pulses in a 512-bit PRBS pattern. Our results reveals that both the SiPhC and SiPhC-GRA waveguides possess the FL and SL spectral regimes, whose dispersion and nonlinearity are enhanced in SL regions, allowing for quantifying the contribution of GV to BER in presence of different number of channels. Meanwhile, the dependence of BER on the waveguide dispersion regimes, namely the normal and anomalous dispersions, has also been addressed in this work. Furthermore, due to the enlarged nonlinear optical parameters in SiPhC-GRA waveguides, their overall BERs are larger than SiPhCs at the same length. Equally important, the acceptable and commensurate BER performance can be achieved in the SiPhCs and SiPhC-GRAs, but with the waveguide length 2.5 times shorter in SL regimes compared to the FL regions. The theoretical models and numerical techniques introduced here can be utilized to explore other optical interconnects or more sophisticated devices in practical applications, paving the ways for the design and construction of the next-generation graphene-based chip-level photonic networks.

Optics EXPRESS

Funding

National Natural Science Foundation of China (11802339, 11804387, 11805276, 11902358, 61801498, 61805282); National University of Defense Technology (ZK16-03-59, ZK18-01-03, ZK18-03-22, ZK18-03-36); Natural Science Foundation of Hunan Province (2016JJ1021); Open Research Fund of Hunan Provincial Key Laboratory of High Energy Technology (GNJGJS03); Opening Foundation of State Key Laboratory of Laser Interaction with Matter (SKLLIM1702); The Youth Talent Lifting Project (17-JCJQ-QT-004).

Disclosures

The authors declare no conflicts of interest.

References

1. J. A. Kash, A. F. Benner, F. E. Doany, D. M. Kuchta, B. G. Lee, P. K. Pepeljugoski, L. Schares, C. L. Schow, and M. Taubenblatt, "Optical interconnects in exascale supercomputers," in *23rd Annual Meeting of the IEEE Photonics Society* (2010), pp. 483–484.
2. Y. A. Vlasov, "Silicon CMOS-integrated nano-photonics for computer and data communications beyond 100G," IEEE Commun. Mag. **50**(2), s67–s72 (2012).
3. S. Abdollahramezani, O. Hemmatyar, H. Taghinejad, A. Krasnok, Y. Kiarashinejad, M. Zandehshahvar, A. Alu, and A. Adibi, "Tunable nanophotonics enabled by chalcogenide phase-change materials," arXiv 2001.06335 (2020).
4. R. Ho, K. W. Mai, and M. A. Horowitz, "The future of wires," Proc. IEEE **89**(4), 490–504 (2001).
5. A. F. Benner, D. M. Kuchta, P. K. Pepeljugoski, R. A. Budd, G. Hougham, B. V. Fasano, K. Marston, H. Bagheri, E. J. Seminaro, H. Xu, D. Meadowcroft, M. H. Fields, L. McColloch, M. Robinson, F. W. Miller, R. Kaneshiro, R. Granger, D. Childers, and E. Childers, "Optics for high-performance servers and supercomputers," in *2010 Conference on Optical Fiber Communication (OFC/NFOEC)*, pp. 1–3.
6. T. Barwicz, H. Byun, F. Gan, C. W. Holzwarth, M. A. Popovic, P. T. Rakich, M. R. Watts, E. P. Ippen, F. X. Kärtner, H. I. Smith, J. S. Orcutt, R. J. Ram, V. Stojanovic, O. O. Olubuyide, J. L. Hoyt, S. Spector, M. Geis, M. Grein, T. Lyszczarz, and J. U. Yoon, "Silicon photonics for compact, energy-efficient interconnects [Invited]," J. Opt. Netw. **6**(1), 63–73 (2007).
7. S.-Y. Lin, E. Chow, V. Hietala, P. R. Villeneuve, and J. D. Joannopoulos, "Experimental Demonstration of Guiding and Bending of Electromagnetic Waves in a Photonic Crystal," Science **282**(5387), 274–276 (1998).
8. R. U. Ahmad, F. Pizzuto, G. S. Camarda, R. L. Espinola, H. Rao, and R. M. Osgood, "Ultracompact corner-mirrors and T-branches in silicon-on-insulator," IEEE Photonics Technol. Lett. **14**(1), 65–67 (2002).
9. B. G. Lee, X. Chen, A. Biberman, X. Liu, I. Hsieh, C. Chou, J. I. Dadap, F. Xia, W. M. J. Green, L. Sekaric, Y. A. Vlasov, R. M. Osgood, and K. Bergman, "Ultrahigh-Bandwidth Silicon Photonic Nanowire Waveguides for On-Chip Networks," IEEE Photonics Technol. Lett. **20**(6), 398–400 (2008).
10. R. M. Osgood, N. C. Panoiu, J. I. Dadap, X. Liu, X. Chen, I. W. Hsieh, E. Dulkeith, W. M. J. Green, and Y. A. Vlasov, "Engineering nonlinearities in nanoscale optical systems: physics and applications in dispersion-engineered silicon nanophotonic wires," Adv. Opt. Photonics **1**(1), 162–235 (2009).
11. J. S. Orcutt, A. Khilo, C. W. Holzwarth, M. A. Popović, H. Li, J. Sun, T. Bonifield, R. Hollingsworth, F. X. Kärtner, H. I. Smith, V. Stojanović, and R. J. Ram, "Nanophotonic integration in state-of-the-art CMOS foundries," Opt. Express **19**(3), 2335–2346 (2011).
12. J. You and N. C. Panoiu, "BER in Slow-Light and Fast-Light Regimes of Silicon Photonic Crystal Waveguides: A Comparative Study," IEEE Photonics Technol. Lett. **29**(13), 1093–1096 (2017).
13. J. You and N. C. Panoiu, "Exploiting high-order phase-shift keying modulation and direct-detection in silicon photonic systems," Opt. Express **25**(8), 8611–8624 (2017).
14. Q. Xu, B. Schmidt, S. Pradhan, and M. Lipson, "Micrometre-scale silicon electro-optic modulator," Nature **435**(7040), 325–327 (2005).
15. R. L. Espinola, J. I. Dadap, R. M. Osgood, S. J. McNab, and Y. A. Vlasov, "Raman amplification in ultrasmall silicon-on-insulator wire waveguides," Opt. Express **12**(16), 3713–3718 (2004).
16. S. Assefa, F. Xia, W. M. J. Green, C. L. Schow, A. V. Rylyakov, and Y. A. Vlasov, "CMOS-Integrated Optical Receivers for On-Chip Interconnects," IEEE J. Sel. Top. Quantum Electron. **16**(5), 1376–1385 (2010).
17. S. Zlatanovic, J. S. Park, S. Moro, J. M. C. Boggio, I. B. Divliansky, N. Alic, S. Mookherjea, and S. Radic, "Mid-infrared wavelength conversion in silicon waveguides using ultracompact telecom-band-derived pump source," Nat. Photonics **4**(8), 561–564 (2010).
18. B. G. Lee, A. Biberman, P. Dong, M. Lipson, and K. Bergman, "All-Optical Comb Switch for Multiwavelength Message Routing in Silicon Photonic Networks," IEEE Photonics Technol. Lett. **20**(10), 767–769 (2008).
19. Y. Hu, T. Jiang, J. Zhou, H. Hao, H. Sun, H. Ouyang, M. Tong, Y. Tang, H. Li, J. You, X. Zheng, Z. Xu, and X. Cheng, "Ultrafast terahertz transmission/group delay switching in photoactive WSe2-functionalized metaphotonic devices," Nano Energy **68**, 104280 (2020).

Optics EXPRESS

20. T. Baba, "Slow light in photonic crystals," Nat. Photonics **2**(8), 465–473 (2008).
21. Y. A. Vlasov and S. J. McNab, "Losses in single-mode silicon-on-insulator strip waveguides and bends," Opt. Express **12**(8), 1622–1631 (2004).
22. E. Dulkeith, F. Xia, L. Schares, W. M. J. Green, and Y. A. Vlasov, "Group index and group velocity dispersion in silicon-on-insulator photonic wires," Opt. Express **14**(9), 3853–3863 (2006).
23. H. K. Tsang, C. S. Wong, T. K. Liang, I. E. Day, S. W. Roberts, A. Harpin, J. Drake, and M. Asghari, "Optical dispersion, two-photon absorption and self-phase modulation in silicon waveguides at 1.5 μm wavelength," Appl. Phys. Lett. **80**(3), 416–418 (2002).
24. T. K. Liang, L. R. Nunes, T. Sakamoto, K. Sasagawa, T. Kawanishi, M. Tsuchiya, G. R. A. Priem, D. Van Thourhout, P. Dumon, R. Baets, and H. K. Tsang, "Ultrafast all-optical switching by cross-absorption modulation in silicon wire waveguides," Opt. Express **13**(19), 7298–7303 (2005).
25. C. Manolatou and M. Lipson, "All-optical silicon modulators based on carrier injection by two-photon absorption," J. Lightwave Technol. **24**(3), 1433–1439 (2006).
26. J. You, S. Lavdas, and N. C. Panoiu, "Theoretical Comparative Analysis of BER in Multi-Channel Systems With Strip and Photonic Crystal Silicon Waveguides," IEEE J. Sel. Top. Quantum Electron. **22**(2), 63–72 (2016).
27. H. Jang, Y. J. Park, X. Chen, T. Das, M.-S. Kim, and J.-H. Ahn, "Graphene-Based Flexible and Stretchable Electronics," Adv. Mater. **28**(22), 4184–4202 (2016).
28. N. Song, X. Gao, Z. Ma, X. Wang, Y. Wei, and C. Gao, "A review of graphene-based separation membrane: Materials, characteristics, preparation and applications," Desalination **437**, 59–72 (2018).
29. C. Chung, Y.-K. Kim, D. Shin, S.-R. Ryoo, B. H. Hong, and D.-H. Min, "Biomedical Applications of Graphene and Graphene Oxide," Acc. Chem. Res. **46**(10), 2211–2224 (2013).
30. A. Nag, A. Mitra, and S. C. Mukhopadhyay, "Graphene and its sensor-based applications: A review," Sens. Actuators, A **270**, 177–194 (2018).
31. M. S. Romano, N. Li, D. Antiohos, J. M. Razal, A. Nattestad, S. Beirne, S. Fang, Y. Chen, R. Jalili, G. G. Wallace, R. Baughman, and J. Chen, "Carbon Nanotube – Reduced Graphene Oxide Composites for Thermal Energy Harvesting Applications," Adv. Mater. **25**(45), 6602–6606 (2013).
32. S. AbdollahRamezani, K. Arik, S. Farajollahi, A. Khavasi, and Z. Kavehvash, "Beam manipulating by gate-tunable graphene-based metasurfaces," Opt. Lett. **40**(22), 5383–5386 (2015).
33. K. Arik, O. Hemmatyar, and Z. Kavehvash, "Beam Manipulation by Hybrid Plasmonic-Dielectric Metasurfaces," Plasmonics, 1–7 (2019).
34. O. Hemmatyar, B. Rahmani, A. Bagheri, and A. Khavasi, "Phase Resonance Tuning and Multi-Band Absorption Via Graphene-Covered Compound Metallic Gratings," IEEE J. Quantum Electron. **53**(5), 1–10 (2017).
35. C.-H. Chang, T.-C. Huang, C.-W. Peng, T.-C. Yeh, H.-I. Lu, W.-I. Hung, C.-J. Weng, T.-I. Yang, and J.-M. Yeh, "Novel anticorrosion coatings prepared from polyaniline/graphene composites," Carbon **50**(14), 5044–5051 (2012).
36. K. S. Novoselov, A. K. Geim, S. V. Morozov, D. Jiang, Y. Zhang, S. V. Dubonos, I. V. Grigorieva, and A. A. Firsov, "Electric Field Effect in Atomically Thin Carbon Films," Science **306**(5696), 666–669 (2004).
37. K. S. Novoselov, A. K. Geim, S. V. Morozov, D. Jiang, M. I. Katsnelson, I. V. Grigorieva, S. V. Dubonos, and A. A. Firsov, "Two-dimensional gas of massless Dirac fermions in graphene," Nature **438**(7065), 197–200 (2005).
38. I. Meric, M. Y. Han, A. F. Young, B. Ozyilmaz, P. Kim, and K. L. Shepard, "Current saturation in zero-bandgap, top-gated graphene field-effect transistors," Nat. Nanotechnol. **3**(11), 654–659 (2008).
39. J. W. You, J. You, M. Weismann, and N. C. Panoiu, "Double-resonant enhancement of third-harmonic generation in graphene nanostructures," Philos. Trans. R. Soc., A **375**(2090), 20160313 (2017).
40. K. I. Bolotin, K. J. Sikes, Z. Jiang, M. Klima, G. Fudenberg, J. Hone, P. Kim, and H. L. Stormer, "Ultrahigh electron mobility in suspended graphene," Solid State Commun. **146**(9-10), 351–355 (2008).
41. X.-H. Deng, J.-T. Liu, J. Yuan, T.-B. Wang, and N.-H. Liu, "Tunable THz absorption in graphene-based heterostructures," Opt. Express **22**(24), 30177–30183 (2014).
42. E. Hendry, P. J. Hale, J. Moger, A. K. Savchenko, and S. A. Mikhailov, "Coherent Nonlinear Optical Response of Graphene," Phys. Rev. Lett. **105**(9), 097401 (2010).
43. R. Miao, Z. Shu, Y. Hu, Y. Tang, H. Hao, J. You, X. Zheng, X. A. Cheng, H. Duan, and T. Jiang, "Ultrafast nonlinear absorption enhancement of monolayer MoS2 with plasmonic Au nanoantennas," Opt. Lett. **44**(13), 3198–3201 (2019).
44. C. Donnelly and D. T. H. Tan, "Ultra-large nonlinear parameter in graphene-silicon waveguide structures," Opt. Express **22**(19), 22820–22830 (2014).
45. T. Gu, N. Petrone, J. F. McMillan, A. van der Zande, M. Yu, G. Q. Lo, D. L. Kwong, J. Hone, and C. W. Wong, "Regenerative oscillation and four-wave mixing in graphene optoelectronics," Nat. Photonics **6**(8), 554–559 (2012).
46. C. H. Kwok and C. Lin, "Polarization-insensitive all-optical NRZ-to-RZ format conversion by spectral filtering of a cross phase modulation broadened signal spectrum," IEEE J. Sel. Top. Quantum Electron. **12**(3), 451–458 (2006).
47. T. P. White, L. O'Faolain, J. Li, L. C. Andreani, and T. F. Krauss, "Silica-embedded silicon photonic crystal waveguides," Opt. Express **16**(21), 17076–17081 (2008).
48. C. Monat, M. Ebnali-Heidari, C. Grillet, B. Corcoran, B. J. Eggleton, T. P. White, L. O'Faolain, J. Li, and T. F. Krauss, "Four-wave mixing in slow light engineered silicon photonic crystal waveguides," Opt. Express **18**(22), 22915–22927 (2010).

Optics EXPRESS

49. S. Lavdas and N. C. Panoiu, "Theory of pulsed four-wave mixing in one-dimensional silicon photonic crystal slab waveguides," Phys. Rev. B **93**(11), 115435 (2016).
50. P. E. Barclay, K. Srinivasan, and O. Painter, "Nonlinear response of silicon photonic crystal microresonators excited via an integrated waveguide and fiber taper," Opt. Express **13**(3), 801–820 (2005).
51. N. C. Panoiu, J. F. McMillan, and C. W. Wong, "Theoretical Analysis of Pulse Dynamics in Silicon Photonic Crystal Wire Waveguides," IEEE J. Sel. Top. Quantum Electron. **16**(1), 257–266 (2010).
52. S. G. Johnson and J. D. Joannopoulos, "Block-iterative frequency-domain methods for Maxwell's equations in a planewave basis," Opt. Express **8**(3), 173–190 (2001).
53. E. H. Hwang and S. Das Sarma, "Dielectric function, screening, and plasmons in two-dimensional graphene," Phys. Rev. B **75**(20), 205418 (2007).
54. F. H. L. Koppens, D. E. Chang, and F. J. García de Abajo, "Graphene Plasmonics: A Platform for Strong Light–Matter Interactions," Nano Lett. **11**(8), 3370–3377 (2011).
55. M. Weismann and N. C. Panoiu, "Theoretical and computational analysis of second- and third-harmonic generation in periodically patterned graphene and transition-metal dichalcogenide monolayers," Phys. Rev. B **94**(3), 035435 (2016).
56. J. L. Cheng, N. Vermeulen, and J. E. Sipe, "Third order optical nonlinearity of graphene," New J. Phys. **16**(5), 053014 (2014).
57. E. Forestieri and M. Secondini, "On the Error Probability Evaluation in Lightwave Systems With Optical Amplification," J. Lightwave Technol. **27**(6), 706–717 (2009).
58. J. You and N. C. Panoiu, "Bit-error ratio calculation for single-channel silicon optical interconnects utilizing return-to-zero pulsed signals," J. Opt. Soc. Am. B **35**(5), 1011–1019 (2018).
59. R. Holzlohner, C. R. Menyuk, W. L. Kath, and V. S. Grigoryan, "Efficient and accurate computation of eye diagrams and bit-error rates in a single-channel CRZ system," IEEE Photonics Technol. Lett. **14**(8), 1079–1081 (2002).
60. R. Holzlohner, C. Menyuk, V. Grigoryan, and W. Kath, "A Covariance Matrix Method for Calculating Accurate Bit Error Rates in a DWDM Chirped RZ System," in *Optical Fiber Communication Conference*, Technical Digest (Optical Society of America, 2003), paper ThW3.
61. C. Helstrom, "Distribution of the filtered output of a quadratic rectifier computed by numerical contour integration," IEEE Trans. Inf. Theory **32**(4), 450–463 (1986).